Acoustic Mode Decomposition in Rectangular Ducts with Sheared Flow

Alexander N. Carr*
NASA Langley Research Center, Hampton, VA, 23681-2199

The performance of new acoustic liner concepts are, in general, characterized and assessed in grazing flow rigs early in the development cycle. These test rigs expose an acoustic liner sample, installed on the side wall of the duct, to a grazing flow and incident acoustic field. The process to characterize these liners involves educing the impedance on the wall where the sample is installed and examining the acoustic power attenuation. Standard approaches to computing impedance or power attenuation generally consider only the effects of a 2D shear flow or uniform flow, on the acoustic field. In this study, the objective is to incorporate 3D shear flow effects in the analysis of acoustic mode attenuation in a rectangular duct flow rig. A modal analysis of microphone measurements obtained on the side walls of the duct upstream and downstream of the test section of the rig is developed. A Galerkin projection of the Pridmore-Brown equation is performed with Chebyshev basis functions in order to incorporate the effects of the Mach number profile on the computation of the axial wavenumber of each mode. Measurements of the Mach number profile are obtained in the test rig and used as input to compute the modes. Comparisons made between the sound field computed with traditional convective Helmholtz modes and the new procedure using Pridmore-Brown modes indicate that the computed acoustic field using Pridmore-Brown modes more accurately reconstructs the acoustic signal at each microphone in the array. The mode structure of the lowest-order mode is shown to be significantly impacted by shear flow refraction effects, and higher-order mode structures are also affected at higher frequencies and centerline Mach number. An assessment of the acoustic mode attenuation for two acoustic liner samples demonstrates that the computed mode amplitudes for both the traditional and new approach are in agreement for the lowest-order mode, but discrepancies arise when higher-order modes are the dominant component of the acoustic field.

Nomenclature

a_{mn}	=	eigenvectors of Pridmore-Brown modes; amplitude coefficients of convective Helmholtz modes
$\mathbf{a}$	=	a_{mn} in vector form
c	=	speed of sound
d	=	diameter of liner facesheet holes
d_y	=	dimension of duct in y-coordinate
d_z	=	dimension of duct in z-coordinate
E_{phase}	=	reconstruction error of microphone phases
E_{SPL}	=	reconstruction error of microphone sound pressure levels
f	=	frequency
h	=	cavity depth of liner samples
i	=	$\sqrt{-1}$
j	=	index of Pridmore-Brown mode
k	=	free-space wavenumber
L	=	number of microphone measurements used in mode decomposition
m	=	order of basis function in y-coordinate
M	=	Mach number
M_c	=	centerline Mach number

*Research Aerospace Engineer, Aeroacoustics Branch, MS 461, AIAA Member.

$\tilde{M}$	=	maximum order of basis function used in y-coordinate
$\mathcal{M}_{mn,m'n'}$	=	components of Galerkin matrix
$\mathcal{M}$	=	Galerkin projection matrix
n	=	order of basis function in z-coordinate
$\mathbf{n}$	=	wall-normal vector
$\tilde{N}$	=	maximum order of basis function in z-coordinate
p	=	acoustic pressure
P	=	acoustic pressure phasor, $P = P(x, y, z, \omega)$
$\hat{p}$	=	acoustic pressure shape function, $\hat{p} = \hat{p}(x, y; \kappa, \omega)$
s	=	arc length between two phasors along the unit circle
s^c	=	complement of s, $s^c = 2\pi - s$
SPL	=	sound pressure level
T_m	=	Chebyshev polynomial of the first kind of order m
$\mathcal{T}$	=	transfer matrix for acoustic mode decomposition
U_m	=	Chebyshev polynomial of the second kind of order m
(x, y, z)	=	three-dimensional Cartesian coordinates
$\mathbf{x}$	=	eigenvector of the generalized eigenvalue problem
Z	=	specific acoustic impedance
ζ	=	normalized specific acoustic impedance
θ	=	phase of acoustic signal
κ	=	axial wavenumber
λ	=	eigenvalue of the generalized eigenvalue problem
μ	=	current guess of κ in the method of successive linear problems
μ_0	=	initial guess of κ
ρ	=	fluid density
ϕ	=	test function
χ_j	=	amplitude coefficients of Pridmore-Brown modes
ψ_{mn}	=	basis function of rectangular duct normal modes
ω	=	radial frequency

I. Introduction

Increasingly stringent noise regulations and rising air traffic demands have fueled a continually growing interest in aircraft noise reduction technology. In subsonic aircraft, a significant component of the overall aircraft noise is fan noise from the turbofan engine. Acoustic liners have traditionally been installed in the walls of the inlet and aft duct to mitigate fan noise. These liners are designed to achieve a target specific acoustic impedance, or impedance for short, that most effectively attenuates the fan noise propagating out of the duct. Achieving a target impedance for new engine designs that meets or exceeds noise reduction expectations requires (1) novel acoustic liner designs, (2) improved impedance optimization technology, and (3) improved experimental analysis methods. This investigation is focused on the third topic, improving experimental analysis techniques, by incorporating shear flow effects into an acoustic mode decomposition approach for analyzing mode attenuation caused by acoustic liners in rectangular duct flow rigs.

The effect of mean flow on the propagation of sound in a duct is commonly considered in the case of constant Mach number plug flow, where a simple dispersion relation may be obtained for the axial wavenumbers of each mode. In this situation, the Ingard-Myers boundary condition [1, 2] is prescribed at an impedance surface. The Ingard-Myers boundary condition assumes a boundary layer of infinitesimal thickness, but instabilities occur when this boundary condition is used in time-domain simulations [3]. A regularized form of this boundary condition may be used by incorporating a small but finite boundary layer thickness [4]. This boundary condition has been successfully implemented in a 2D impedance eduction technique [5]. Other impedance eduction techniques have incorporated shear flow effects in 2D [6–8]. However, the boundary layer thickness will vary with the spanwise coordinate in a 3D duct, particularly near the corners. The inability of boundary conditions to account for 3D shear flow effects is a significant reason for the desire to develop 3D analysis techniques that account for shear flow effects on acoustic propagation. Recent studies have also shown different educed impedances for the same liner sample when the direction of acoustic propagation relative to the flow direction is altered [8, 9]. Accounting for 3D flow effects may provide further insight on this phenomenon, as 2D shear flow impedance eduction methods ignore the effect of corners, which likely cannot be neglected for the small

duct cross-sections in flow rigs used for impedance eduction.

Impedance eduction at the NASA Langley Research Center is performed in the Grazing Flow Impedance Tube (GFIT) at frequencies below the first cut-on frequency. Thus, there is not only a desire to incorporate 3D shear flow effects, but also more complicated acoustic fields with multiple modes into the impedance eduction capabilities. The natural first step to accomplish this is to develop a technique for incorporating 3D shear flow effects on acoustic mode decomposition. Acoustic mode decomposition is performed in the NASA Langley Curved Duct Test Rig (CDTR) to assess the mode attenuation caused by liner samples. Modal decomposition techniques have been categorized by Åbom [10] to fall under the purview of direct techniques and correlation techniques. Direct techniques rely on direct measurements of an acoustic field quantity at several locations, whereas correlation techniques rely upon a space-time correlation of an acoustic field quantity at several locations. Much of the early development of these techniques focused on fan noise characterization, and thus were developed for circular or annular ducts. Mugridge [11] was one of the first investigators to use modal decomposition to analyze acoustic propagation in a duct. A cross-correlation technique was applied to hot-wire measurements of the axial acoustic particle velocity to extract the modes present in the duct at appropriate blade passing frequencies. Several investigations followed that applied the cross-correlation approach to microphone measurements [12, 13]. Moore [14] introduced a direct technique to extract duct modes, and subsequent investigators [10, 15–19] performed independent investigations with a direct approach. For both approaches, the modes may be determined by performing a spatial Fourier transform over a cross-section of the duct or by solving a linear system relating an assumed form of the solution to microphone measurements. Pickett et al. [15] showed that a least-squares regression solution to the linear system approach minimizes the sensitivity of the computed modes to measurement errors. Åbom [10] generalized the modal decomposition approach to compute incident and reflected modes, such that measurements of the reflection matrix may be performed. This is a very useful tool in the analysis of acoustic liners, as Schultz et al. [19] have shown that the frequency range of the impedance tube problem may be extended beyond the first cut-on frequency of the test apparatus with a modal decomposition analysis.

The previous investigations discussed here involving modal decomposition have either ignored flow effects or assumed constant Mach number plug flow. Åbom [10] briefly discussed the possibility of errors being introduced in measurements that ignore shear flow effects, and urged caution in the application of this simplified flow model. An interesting point raised was the apparent discrepancy in the results of Savkar [20], which suggest that the plane wave mode is most affected by the presence of shear layers, with the suggestion of Salikuddin and Ramakrishnan [18] that the higher-order modes would be most affected by nonuniformity in the flow. An investigation by Boucheron et al. [21], assuming a laminar mean flow in a circular duct, has shown that pressure profiles of all modes are affected by refraction caused by the presence of shear flow, and that this refraction effect has increasing importance as the Mach number and frequency are increased.

An objective of the present investigation is to establish a modal decomposition method that accounts for the effects of shear flow, so that acoustic mode attenuation of liner samples may be more accurately computed and understanding of liner performance may be improved. To perform such an analysis, flow profile measurements are performed in the CDTR. The experimental setup is presented in Sec. II. The theory and approach taken to perform the modal decomposition in the CDTR is outlined in Sec. III. In Sec. IV, results are presented for the Mach number flow profiles and modal decomposition analysis performed in the CDTR for several acoustic liner test samples. In Sec. V, conclusions of the work and future investigations are discussed.

II. Experimental Setup

The NASA Langley CDTR is an open loop wind tunnel with a centrifugal fan that draws in air from the atmosphere through a 6 in $\times$ 15 in (15.24 cm $\times$ 38.10 cm) rectangular duct test section. Figure 1 shows an illustration of the CDTR. The CDTR can reach speeds of $M_c = 0.5$, where M_c denotes the centerline Mach number. It is designed to assess the acoustic and aerodynamic performance of acoustic liner test samples, and the test section ranges between 100% and 25% of the scale of the aft bypass duct of a business jet or large commercial passenger aircraft turbofan engine, respectively. Acoustic liners may be installed in both of the 15 in walls in the test section. Sound is generated using an array of 32 loudspeakers, which can be placed either upstream (aft mode) or downstream of the test section (inlet mode). Tonal or broadband sound may be generated by the array in the frequency range of 400 to 3000 Hz. Due to the large cross-section of the duct, many modes are cut-on across the frequency range of interest. The exact number depends on environmental factors, such as static temperature and relative humidity, that cannot be controlled in the CDTR and affect the sound speed. As an example, a recent test conducted at $M_c = 0.45$ found 22 modes cut-on at 3000 Hz [22]. The CDTR also has mode control capabilities for constant Mach number normal modes; a single mode amplitude may

be increased relative to all other present modes by varying the amplitude and phase of each driver in the loudspeaker array individually. This makes the CDTR an excellent candidate for the implementation of a modal decomposition approach that incorporates shear flow effects, since we may examine the effects of shear flow on many acoustic modes.

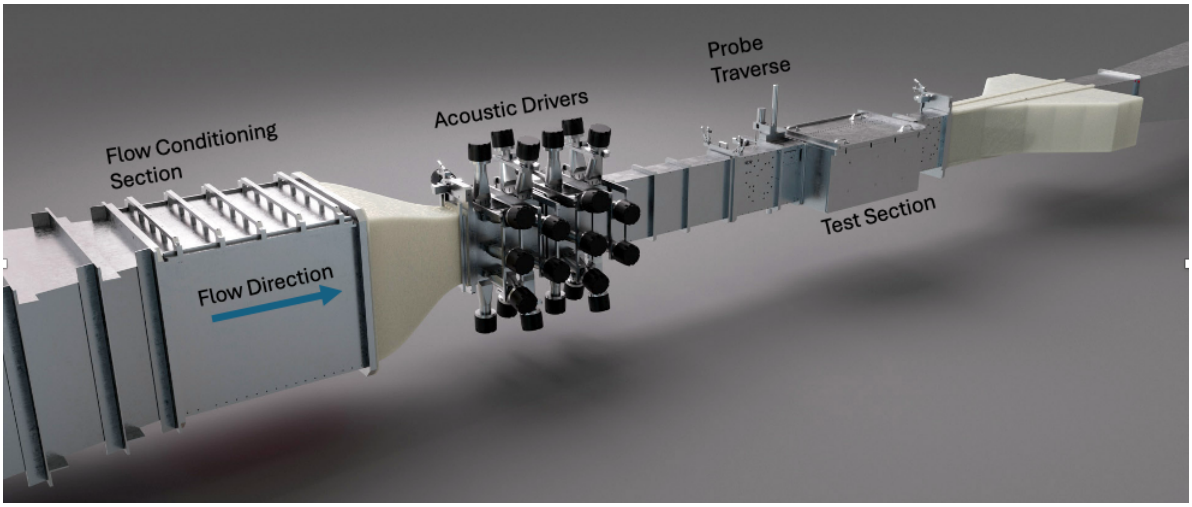

Fig. 1 Rendering of the CDTR with key components labeled.

A. Flow Profile Measurements

Measurements of the Mach number in the transverse plane just upstream of the test section are performed with a total pressure probe at 506 locations. A single port on the centerline of the duct lower wall, in-plane with the total pressure probe tip, is used to measure static pressure. The centerline Mach number is set to 0.1, 0.3, and 0.5. Measurement points are clustered near the walls and corners, as shown in Fig. 2, in order to capture the Mach number gradients in the boundary layer and corners. The probe is not able to get closer than 0.635 cm to the upper and lower walls of the duct due to physical constraints. Future research will examine the boundary layer in the upper and lower walls, as well as perform flow profile measurements downstream of the test section. Unfortunately, due to a bearing seal failure in the CDTR fan during testing, these measurements are not available for this investigation.

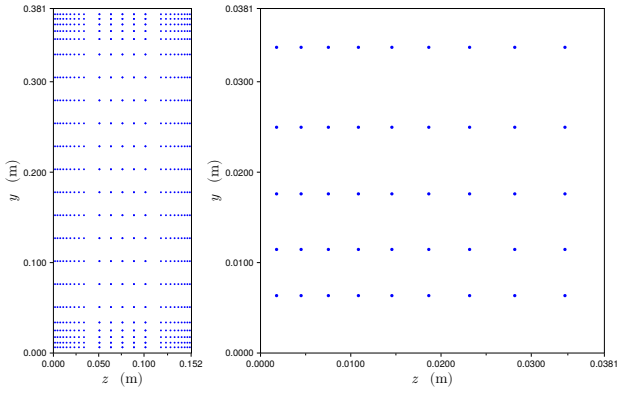

Fig. 2 Measurement locations of the Mach number in the duct cross-section just upstream of the test section. Additional zoomed in view of measurement points in lower left-hand corner provided.

B. Acoustic Mode Decomposition Study

The effect of shear flow on acoustic mode decomposition and attenuation in the CDTR is investigated by extracting the acoustic modes in the upstream and downstream microphone arrays in the case of (1) a CDTR3 liner sample, and (2)

a CDTR5 liner sample. The two liner samples are perforate-over-honeycomb configurations whose dimensions are provided in Table 1. The dimensions provided are; percent open area (POA), facesheet thickness (t), cavity depth (h), and hole diameter (d). Both the modal attenuation of traditional normal modes (assuming constant Mach number), and the Pridmore-Brown acoustic modes, are computed. Tonal sound from 400 Hz to 3000 Hz is generated, and a mode control algorithm varies the phase of the signals provided to each loudspeaker in the array in order to amplify a single normal mode in the duct. The liner samples are only installed in one wall of the test section, not both walls.

Table 1 Dimensions of two CDTR liner samples.

Sample	POA	t (in)	h (in)	d (in)
CDTR3	15.3	0.040	1.569	0.093
CDTR5	12.8	0.040	0.732	0.036

III. Modal Analysis

The domain of interest is a rectangular duct of constant cross-section, with dimensions d_y and d_z, as described by the diagram in Fig. 3. We assume that the duct contains plane parallel shear flow and the Mach number is a function of the transverse coordinates, denoted $M = M(y, z)$. Although the flow in the CDTR is not fully developed, the portion of the duct where modal decomposition is performed is small compared to the overall length. Thus, an assumption is made that the flow may be assumed fully developed in the mode decomposition calculations. At each boundary, the wall is prescribed a normalized specific acoustic impedance, ζ.

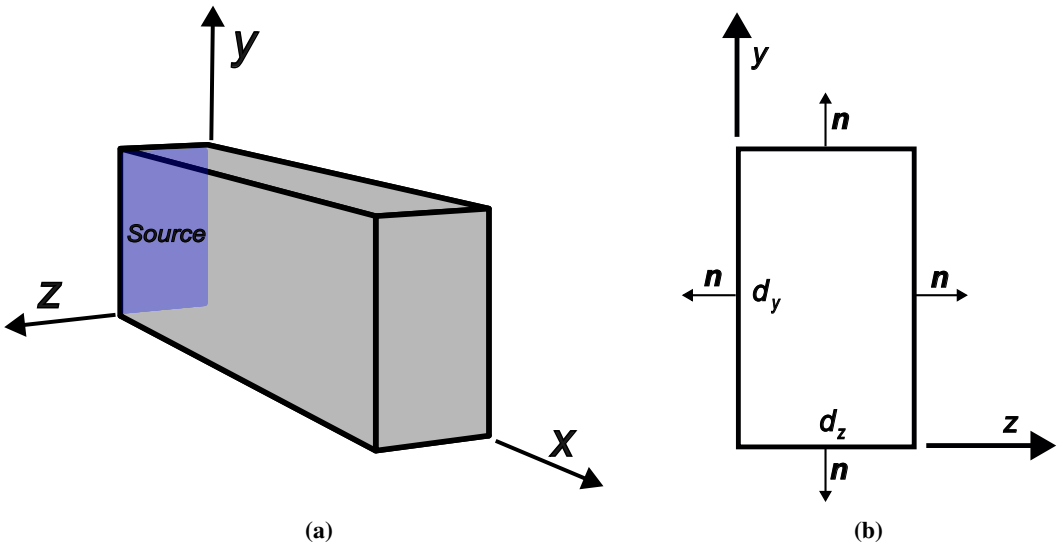

Fig. 3 Diagrams of (a) coordinate system for rectangular duct, and (b) wall-normal vectors along boundary.

The linearized Euler equations govern the propagation of small-amplitude disturbances in a fluid when thermoviscous and molecular relaxation effects may be ignored. Pridmore-Brown [23] showed that, in the situation when the flow direction is aligned with the direction of acoustic propagation, these equations may be combined into a single equation for the acoustic pressure,

$$(k - \kappa M)^2 \nabla \cdot \left(\frac{1}{(k - \kappa M)^2} \nabla \hat{p} \right) + \left[(k - \kappa M)^2 - \kappa^2 \right] \hat{p} = 0, \tag{1}$$

where $p(x, y, z, t) = \hat{p}(y, z; \kappa, \omega) \exp(-i\omega t + i\kappa x)$, $k = 2\pi f c^{-1}$ is the temporal wavenumber, c is the speed of sound, f is the acoustic frequency, and κ is the axial wavenumber. Equation 1 is referred to as the Pridmore-Brown equation

(PBE). On the duct walls, the acoustic pressure satisfies the Ingard-Myers boundary condition [1, 2]

$$\nabla\hat{p}\cdot\mathbf{n}+\frac{(k-\kappa M)^2}{ik\zeta}\hat{p}=0, \tag{2}$$

where $\zeta = Z/\rho c$ is the normalized specific acoustic impedance, Z is the specific acoustic impedance, and ρ is the fluid density. We define the unit normal vector, $\mathbf{n}$, to point outwards from the boundary of the duct as in Fig. 3b. To be precise, the boundary conditions at each surface are

$$\left[\frac{\partial\hat{p}}{\partial y}-\frac{(k-\kappa M)^2}{ik\zeta}\hat{p}\right]_{y=0}=0, \tag{3}$$

$$\left[\frac{\partial\hat{p}}{\partial y}+\frac{(k-\kappa M)^2}{ik\zeta}\hat{p}\right]_{y=d_y}=0, \tag{4}$$

$$\left[\frac{\partial\hat{p}}{\partial z}-\frac{(k-\kappa M)^2}{ik\zeta}\hat{p}\right]_{z=0}=0, \tag{5}$$

and

$$\left[\frac{\partial\hat{p}}{\partial z}+\frac{(k-\kappa M)^2}{ik\zeta}\hat{p}\right]_{z=d_z}=0. \tag{6}$$

In the case of hard walls, $\zeta\to\infty$, the boundary conditions reduce to the usual Neumann conditions for the acoustic pressure. For soft walls, $\zeta\to 0$, the boundary conditions are Dirichlet (i.e., $\hat{p}=0$). In the general formulation of the problem, the Ingard-Myers boundary condition provides flexibility in the sense that a vanishing thin boundary layer may be assumed. However, in practice, a no-slip boundary condition exists at the walls of the duct. By setting $M=0$ at the walls, Eq. 2 automatically satisfies this condition, and no change to the formulation in Sec. III.A is required.

The primary difficulty in finding solutions to Eq. 1 is the determination of κ for nonuniform flow. For constant Mach number flow, a simple equation is obtained for the dispersion relation that relates the duct geometry, Mach number, and frequency to the axial wavenumber. When M is a function of the transverse coordinates, no such equation is obtained. Rienstra [24] proposed a Galerkin approach for finding κ in a 2D duct and 3D cylindrical duct. We will extend that approach here to obtain κ for a 3D rectangular duct.

A. Galerkin Projection

We start by expressing Eq. 1 in weak form by multiplying by $\phi(k-\kappa M)^{-2}$ and integrating over the cross-section,

$$\int_0^{d_y}\left.\frac{\phi\hat{p}}{ik\zeta}\right|_{z=d_z}+\left.\frac{\phi\hat{p}}{ik\zeta}\right|_{z=0}\mathrm{d}y+\int_0^{d_z}\left.\frac{\phi\hat{p}}{ik\zeta}\right|_{y=d_y}+\left.\frac{\phi\hat{p}}{ik\zeta}\right|_{y=0}\mathrm{d}z-\int_0^{d_z}\int_0^{d_y}\frac{\nabla_\perp\phi\cdot\nabla_\perp\hat{p}}{(k-\kappa M)^2}-\left[1-\frac{\kappa^2}{(k-\kappa M)^2}\right]\phi\hat{p}\mathrm{d}y\mathrm{d}z=0. \tag{7}$$

The function ϕ is a smooth test function. It should be noted that the factor $\phi(k-\kappa M)^{-2}$ is never equal to zero at any location in the cross-section of the CDTR. This is because only subsonic flow is present, $0\le M<1$, and $\kappa\le k$. Thus, $\kappa M<k$ for all conditions examined here. We now assume a form of the solution for $\hat{p}$,

$$\hat{p}=\sum_{n=0}^{\infty}\sum_{m=0}^{\infty}a_{mn}\psi_{mn}(y,z), \tag{8}$$

and prescribe $\psi_{mn}(y,z)$ to be a Chebyshev basis,

$$\psi_{mn}(y,z)=T_m(\tilde{y})\,T_n(\tilde{z}), \tag{9}$$

where $\tilde{y}=(2/d_y)y-1$ and $\tilde{z}=(2/d_z)z-1$ map the physical coordinates to the Chebyshev domain. Then, we let $\phi=\psi_{m'n'}$ such that the test function is orthogonal with the assumed basis. Upon substitution into Eq. 7, we obtain an

eigenvalue problem for the eigenvalues, κ, and the eigenvectors, a_{mn},

$$\sum_{n=0}^{\infty}\sum_{m=0}^{\infty} a_{mn}\left[\int_0^{d_y}\left(\frac{(-1)^{n'}(-1)^n}{ik\zeta_{z=d_z}}+\frac{1}{ik\zeta_{z=0}}\right)T_{m'}(\tilde{y})\,T_m(\tilde{y})\,\mathrm{d}y+\int_0^{d_z}\left(\frac{(-1)^{m'}(-1)^m}{ik\zeta_{y=d_y}}+\frac{1}{ik\zeta_{y=0}}\right)T_{n'}(\tilde{z})\,T_n(\tilde{z})\,\mathrm{d}z\right.$$
$$-\int_0^{d_z}\int_0^{d_y}\frac{1}{(k-\kappa M)^2}\left(\frac{4mm'}{d_y^2}U_{m'-1}(\tilde{y})\,U_{m-1}(\tilde{y})\,T_{n'}(\tilde{z})\,T_n(\tilde{z})+\frac{4nn'}{d_z^2}U_{n'-1}(\tilde{z})\,U_{n-1}(\tilde{z})\,T_{m'}(\tilde{y})\,T_m(\tilde{y})\right)$$
$$\left.-\left(1-\frac{\kappa^2}{(k-\kappa M)^2}\right)T_{n'}(\tilde{z})\,T_n(\tilde{z})\,T_{m'}(\tilde{y})\,T_m(\tilde{y})\,\mathrm{d}y\mathrm{d}z\right]=0. \quad (10)$$

Assuming $\tilde{M}$ polynomials will be used for m and m', and $\tilde{N}$ polynomials for n and n', the matrix size is $\tilde{M}\tilde{N}\times\tilde{M}\tilde{N}$.

Let the expression in brackets in Eq. 10 be a matrix with each element denoted by $\mathcal{M}_{mn,m'n'}(\kappa)$, where mn varies along the columns and $m'n'$ varies along the rows. Thus, we have

$$\begin{bmatrix}\mathcal{M}_{00,00} & \mathcal{M}_{10,00} & \cdots & \mathcal{M}_{01,00} & \cdots & \mathcal{M}_{\tilde{M}\tilde{N},00}\\ \mathcal{M}_{00,10} & \ddots & & & & \vdots\\ \vdots & & \ddots & & & \vdots\\ \mathcal{M}_{00,01} & & & \ddots & & \vdots\\ \vdots & & & & \ddots & \vdots\\ \mathcal{M}_{00,\tilde{M}\tilde{N}} & \cdots & \cdots & \cdots & \cdots & \mathcal{M}_{\tilde{M}\tilde{N},\tilde{M}\tilde{N}}\end{bmatrix}\begin{bmatrix}a_{00}\\ a_{10}\\ \vdots\\ a_{01}\\ \vdots\\ a_{MN}\end{bmatrix}=0, \quad (11)$$

or $\mathcal{M}(\kappa)\,\mathbf{a}=0$ for short. Equation 11 is a nonlinear eigenvalue problem, because $\mathcal{M}$ depends on κ. Our objective is to find all of the $(\kappa,\mathbf{a})$ pairs that satisfy Eq. 11. Each pair represents a linearly independent solution to Eq. 1. Rienstra [24] demonstrated the ability of the method of successive linear problems in solving Eq. 11 for κ and $\mathbf{a}$.

B. Method of Successive Linear Problems

The method of successive linear problems is an approach for finding the eigenpairs, $(\kappa,\mathbf{a})$, of a nonlinear eigenvalue problem [25]. It is a Newton-like iteration method that requires an initial guess for the eigenvalue. Suppose that there are J eigenpairs that we would like to find. We may note that $\mathcal{M}(\kappa)$ may be linearized about the point μ by retaining the first two terms of a Taylor expansion,

$$\mathcal{M}(\kappa)=\mathcal{M}(\mu)+(\kappa-\mu)\,\mathcal{M}'(\mu), \quad (12)$$

where $\mathcal{M}'(\mu)$ denotes the derivative of $\mathcal{M}(\kappa)$ with respect to κ evaluated at the point μ. The eigenvalue problem may be approximated by linearization,

$$\mathcal{M}(\kappa)\,\mathbf{a}\approx[\mathcal{M}(\mu)+(\kappa-\mu)\,\mathcal{M}'(\mu)]\,\mathbf{a}=0, \quad (13)$$

and this approximation becomes more accurate as μ converges to κ.

The process to obtain the eigenpair closest to our initial guess involves iterating on the generalized eigenvalue problem,

$$\mathcal{M}(\mu)\,\mathbf{x}=-\lambda\mathcal{M}'(\mu)\,\mathbf{x}. \quad (14)$$

We start by making an initial guess, $\mu=\mu_0$, which should be less than the most negative eigenvalue of Eq. 11. Then, by solving Eq. 14, we obtain a set of eigenvalues, λ, and eigenvectors, $\mathbf{x}$. We observe that there exists some κ that will satisfy the relation $\kappa=\mu+\lambda$. Thus, to find the κ closest to our initial guess, we update μ by setting it equal to the previous guess plus the absolute value of the absolutely smallest eigenvalue of the solution to Eq. 14, $\mu=\mu+|\lambda_{\min}|$. The process of solving Eq. 14 and updating μ is repeated until $\|\mathcal{M}(\mu)\,\mathbf{x}\|$ is below some specified tolerance. Then, the eigenpair is stored, $\kappa^{(j)}=\mu$ and $\mathbf{a}^{(j)}=\mathbf{x}$, where j is the index of the eigenpairs that satisfy $\mathcal{M}(\kappa)\,\mathbf{a}=0$, and the process is repeated to find the next eigenpair. The initial guess for the next eigenvalue is obtained by taking the previously obtained κ and adding to it the absolute value of the second smallest eigenvalue obtained from the last iteration of Eq. 14. Ruhe [26] was able to find the maximal number of eigenvalues by using this approach to update the initial guess for the next eigenvalue.

Validation of the method of successive linear problems is performed by computing the eigenvalues of the 2D duct problem outlined in Rienstra [24]. The Ingard-Myers boundary condition is applied at $y = 0$ and $y = d_y$. The mean flow Mach number profile is linear, $M = 0.5 + 0.3(y/d_y)$, and the nondimensional frequency is 20 (see Table 2 of Rienstra [24] for more details on this example case). The number of polynomials used to resolve the y-direction is 20. Thus, the computed wavenumbers should match the results of the 2D solver developed by Rienstra [24]. Gauss-Legendre integration with 81 nodes is performed to compute the integrals in $\mathcal{M}(\kappa)$ and $\mathcal{M}'(\kappa)$. Eighteen cut-on hardwall modes are obtained from this implementation of the method of successive linear problems that agree, to 4 decimal places, with the results presented in Table 2 of Rienstra [24]. Thus, the algorithm described here for solving $\mathcal{M}(\kappa)\,\mathbf{a} = 0$ is validated for a case with previously reported results. The 3D eigenvalue solver was also validated by setting the flow profile to the same profile as the 2D case, such that the variation in z is constant. Then, $\tilde{M}$ was set to 20 and $\tilde{N}$ was set to 1. The computed eigenvalues matched the 2D solver results.

C. Modal Decomposition

The acoustic field in the duct is a linear superposition of all the solutions of Eq. 1,

$$P(x, y, z, \omega) = \sum_{j=1}^{J} \chi_j \sum_{n=0}^{\infty} \sum_{m=0}^{\infty} a_{mn}^{(j)} \psi_{mn}(y, z)\, e^{i\kappa^{(j)} x}, \tag{15}$$

where χ_j are the amplitude coefficients for each $(\kappa, \mathbf{a})$ pair. In practice, the summations are cut-off at the number of polynomials used in the decomposition, $\tilde{M}$ and $\tilde{N}$. Microphone measurements obtained on the duct walls provide L number of $P(x, y, z, \omega)$ values for each frequency. Thus, finding χ_j is a matter of solving $\mathcal{T}\boldsymbol{\chi} = \mathbf{P}$, where $\mathbf{P}$ is a vector of the complex pressures at each microphone, $\boldsymbol{\chi}$ is the vector of amplitude coefficients for each eigenpair, and $\mathcal{T}$ is a matrix of the eigenvectors and basis functions at each microphone location for each eigenpair. In more detail, the matrix equation is

$$\begin{bmatrix} \sum_{n=0}^{\infty}\sum_{m=0}^{\infty} a_{mn}^{(1)}\psi_{mn}(y_1, z_1)\, e^{i\kappa^{(1)}x_1} & \cdots & \sum_{n=0}^{\infty}\sum_{m=0}^{\infty} a_{mn}^{(J)}\psi_{mn}(y_1, z_1)\, e^{i\kappa^{(J)}x_1} \\ \vdots & \ddots & \vdots \\ \sum_{n=0}^{\infty}\sum_{m=0}^{\infty} a_{mn}^{(1)}\psi_{mn}(y_L, z_L)\, e^{i\kappa^{(1)}x_L} & \cdots & \sum_{n=0}^{\infty}\sum_{m=0}^{\infty} a_{mn}^{(J)}\psi_{mn}(y_L, z_L)\, e^{i\kappa^{(J)}x_L} \end{bmatrix} \begin{bmatrix} \chi_1 \\ \vdots \\ \chi_J \end{bmatrix} = \begin{bmatrix} P(x_1, y_1, z_1) \\ \vdots \\ P(x_L, y_L, z_L) \end{bmatrix}. \tag{16}$$

The solution of Eq. 16 is computed by linear least-squares regression.

Once the χ_j are determined, each mode (eigenpair) may be assigned an amplitude or phase. The mode SPL refers to the amplitude of χ_j normalized by the reference pressure in air, $p_{\text{ref}} = 20 \times 10^{-6}$ Pa, reported on a dB scale,

$$\text{SPL}_{\text{mode},j} = 10 \log\left(\frac{\chi_j \chi_j^*}{2p_{\text{ref}}^2}\right). \tag{17}$$

The mode phase corresponds to the argument of χ_j, $\arg(\chi_j)$. As a measure of goodness of the modal decomposition, the computed mode amplitudes may be used in conjunction with Eq. 15 to compute the SPL and phase at each microphone location. Then, the predicted SPL and phase from the mode decomposition may be compared to the measured SPL and phase at each microphone to compute a reconstruction error. The SPL reconstruction error is defined as,

$$E_{\text{SPL,PBE}} = \frac{\|\text{SPL}_{\text{PBE}} - \text{SPL}_{\text{measured}}\|_2}{\|\text{SPL}_{\text{measured}}\|_2}, \tag{18}$$

where $\|\cdot\|_2$ is the Euclidean norm, $\text{SPL}_{\text{measured}}$ is the measured SPL at each microphone, and SPL_{PBE} is the reconstructed SPL at each microphone using PBE modes. The phase reconstruction error is computed as the average of the minimum arc length between the phasor on a unit circle corresponding to the measured phase and the phasor corresponding to the predicted phase, normalized by π,

$$E_{\text{phase,PBE}} = \frac{1}{N_{\text{mics}}} \sum_{i=1}^{N_{\text{mics}}} \frac{\min(s, s^c)}{\pi}, \tag{19}$$

where $s = |\theta_{\text{measured}} - \theta_{\text{PBE}}|$ and $s^c = 2\pi - s$. Thus, a phase error of 1 would imply that the predicted phases are π radians out of phase with the measured results at each microphone, on average.

It is worth discussing briefly some results for the case of a constant Mach number profile. If M is constant in Eq. 1, and $\zeta \to \infty$ in the case of acoustically hard walls, then the most convenient ansatz is to assume a cosine basis

$$\hat{p} = \sum_{n=0}^{\infty} \sum_{m=0}^{\infty} a_{mn} \cos\left(\frac{m\pi}{d_y} y\right) \cos\left(\frac{n\pi}{d_z} z\right). \tag{20}$$

Then, κ satisfies the quadratic equation,

$$(k - \kappa M)^2 - \kappa^2 - \left(\frac{m\pi}{d_y}\right)^2 - \left(\frac{n\pi}{d_z}\right)^2 = 0, \tag{21}$$

and may be determined analytically for each (m, n). A modal decomposition may be performed to determine the mode coefficients, a_{mn}, and the resulting solution corresponds to the solution of the convective Helmholtz equation (CHE). The expression for the mode SPL, Eq. 17, is still valid for CHE modes if χ_j is replaced by a_{mn}. In Sec. IV, results for PBE modes are compared to CHE modes to highlight differences in acoustic propagation resulting from the shear flow in the boundary layer region.

IV. Application to the Curved Duct Test Rig

A. Flow Measurements and Validation

Measurements of the Mach number in the CDTR are performed at $M_c = 0.1$, 0.3, and 0.5 just upstream of the test section at the locations reported in Sec. II. A nonuniform rational basis spline (NURBS) model is then used to create a smooth 2D surface, while assuming that the Mach number at the walls is zero. Next, the Mach number is interpolated onto a 2D Legendre roots grid with 64 points in each direction, which is the grid used to perform Gauss-Legendre quadrature of the integrals in Eq. 10.

Figure 4 displays three contour plots corresponding to $M_c = 0.1$, 0.3, and 0.5. The core region (the region where M is approximately constant and near the centerline value) comprises about half of the area of the duct. The remaining portion is the boundary layer region. The boundary layers on the top and bottom walls experience a vortex roll-up in the center due to the contraction after the flow conditioning section. The boundary layers on the side walls ($z = 0$ and $z = 0.1524$ m) are relatively better behaved, with a boundary layer thickness of approximately 2.54 cm for all M_c. Thus, approximately $1/3$ of the z dimension of the CDTR contains a boundary layer with sheared flow.

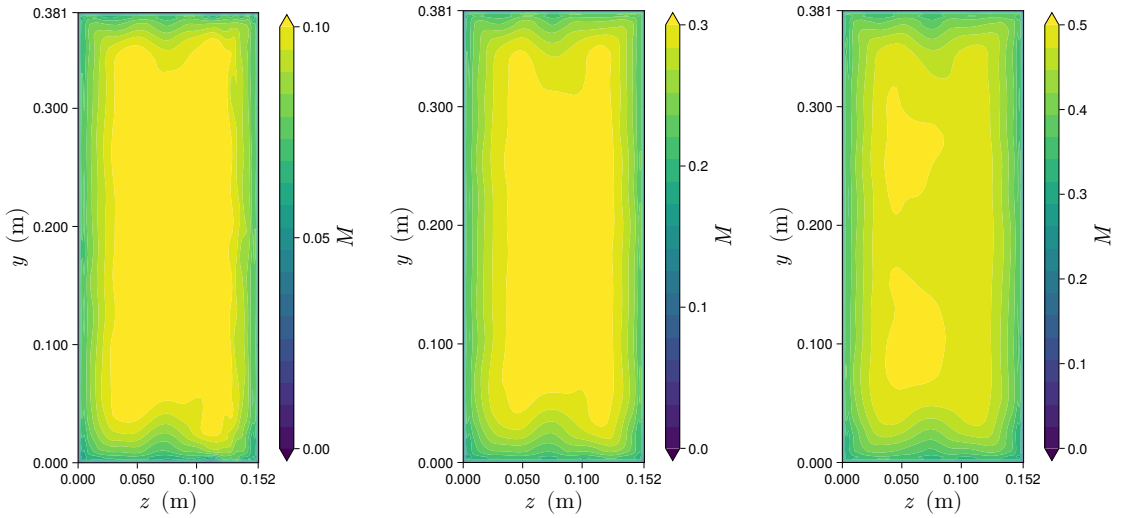

(a) $M_c = 0.1$ **(b)** $M_c = 0.3$ **(c)** $M_c = 0.5$

Fig. 4 Contour plots of the Mach number upstream of the test section.

Once the Mach number profile is known at the Legendre grid points, the eigenpairs are determined and modal decomposition is performed for frequencies ranging from 400 Hz to 3000 Hz. In order to validate the method, and

also determine the appropriate size of $\tilde{M}$ and $\tilde{N}$ required to adequately describe the acoustic field, the SPL and phase reconstruction errors are computed and compared to results from a modal decomposition of the CHE. Figure 5 shows the computed reconstruction errors for $M_c = 0.5$ setpoints where the $(0, 0)$ CHE mode is dominant (Figs. 5a and 5b) and the $(0, 1)$ CHE mode is dominant (Figs. 5c and 5d). As $\tilde{M}$ and $\tilde{N}$ are increased, the eigenvalue solver was able to find more eigenpairs and eventually match the number of wavenumbers determined by the CHE dispersion relation. When all eigenpairs were found, the SPL and phase errors for the PBE mode decomposition converge to approximately the same values as the CHE results for the $(0, 0)$ mode when $f \leq 1200$ Hz. For higher frequencies, the PBE modal reconstruction displays a significant improvement in the phase error for both modes, with exception to the $f = 2200$ Hz case of the $(0, 0)$ CHE mode. The improved phase and SPL reconstruction errors at higher frequencies would appear to indicate a more significant impact of the shear flow on acoustic propagation as the frequency is increased.

One possible reason for the larger PBE reconstruction errors at 2200 Hz may be due to the fact that the method of successive linear problems found one less eigenvalue than the CHE results predicted. This meant that the total number (positive and negative) of PBE modes for this case is an odd number, so one positive mode is missing its corresponding negative mode. An attempt to find the missing eigenvalue was made by altering some parameters of the eigenvalue solver; however, this was unsuccessful. Future investigations will attempt to improve the eigenvalue solver, and perhaps resort to a different method, such as the contour integral method of Beyn [27].

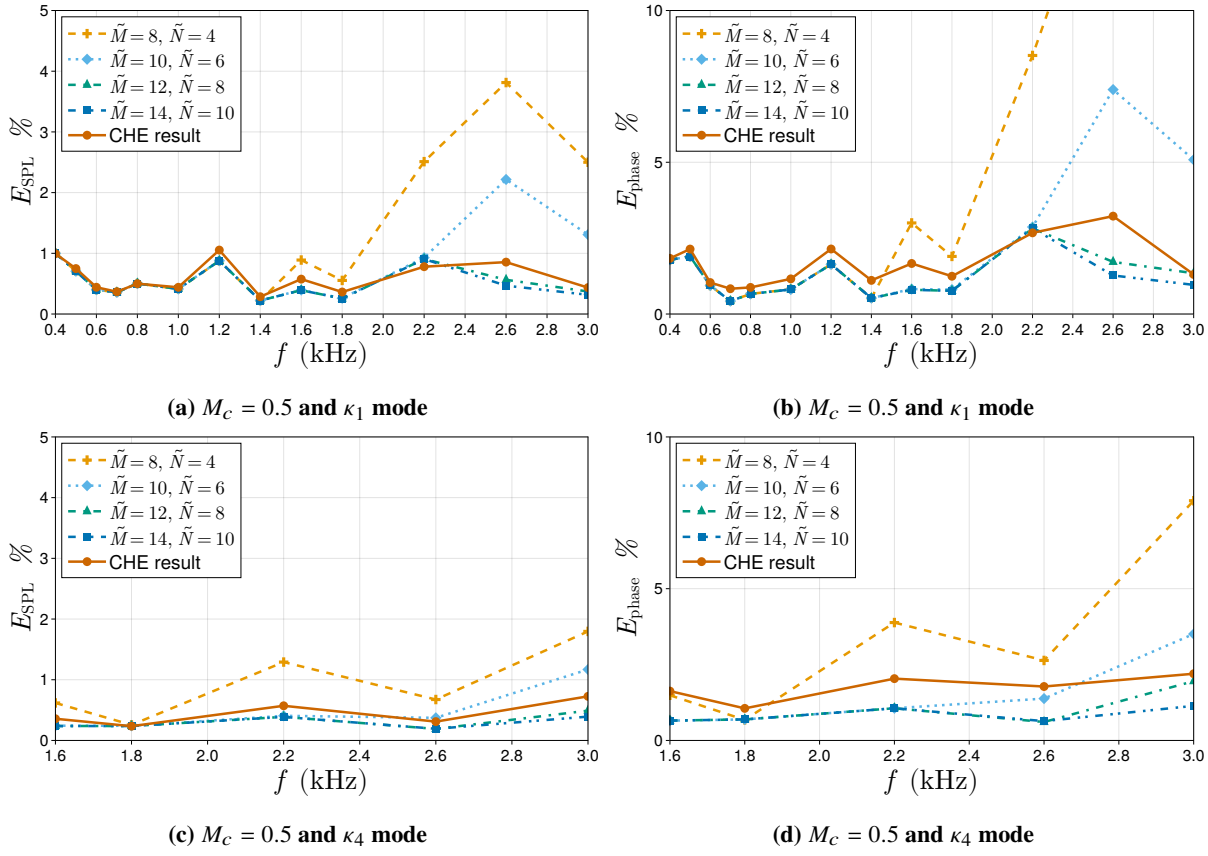

(a) $M_c = 0.5$ **and** κ_1 **mode**

(b) $M_c = 0.5$ **and** κ_1 **mode**

(c) $M_c = 0.5$ **and** κ_4 **mode**

(d) $M_c = 0.5$ **and** κ_4 **mode**

Fig. 5 Microphone reconstruction errors for SPL and phase.

B. Mode Structure

In general, the number of eigenvalues found by the method of successive linear problems matches the number of cut-on modes determined by the CHE dispersion relation. In Table 2, κ is presented for PBE and CHE modes at $f = 1600$ Hz for three different centerline Mach numbers. The PBE mode wavenumbers do not significantly deviate from the CHE wavenumbers for both the postive and negative modes of the $M_c = 0.1$ and 0.3 setpoints. For $M_c = 0.5$, the negative mode PBE wavenumbers deviate more significantly from the CHE wavenumbers than the results for

the positive modes. This appears to suggest a more significant impact of the boundary layer on upstream acoustic propagation, as opposed to downstream propagation. The negative wavenumbers for PBE modes are consistently smaller in absolute magnitude as compared to their CHE counterparts. This results in an increase in the phase speed of the wave in a sheared duct, which would cause the angle of incidence between the wavefront and duct walls to decrease. When this happens, the wave "bounces" between the duct walls more frequently, and the effectiveness of an acoustic liner in attenuating the signal may be increased. A more detailed geometrical description of the relation of phase speed and angle of incidence may be found in Ch. 6 of Blackstock [28].

Table 2 Axial wavenumbers for $f = 1600$ Hz and $M_c = 0.1$, 0.3, and 0.5.

		$M_c = 0.1$		$M_c = 0.3$		$M_c = 0.5$	
PBE mode number	CHE mode number	PBE	CHE	PBE	CHE	PBE	CHE
1	(0,0)	27.057	26.919	23.301	22.950	20.750	20.148
2	(1,0)	25.947	25.748	22.252	21.789	19.736	19.005
3	(2,0)	22.061	21.907	18.373	18.017	15.938	15.356
4	(0,1)	18.706	18.582	15.081	14.812	12.795	12.356
5	(1,1)	17.117	16.927	13.647	13.244	11.523	10.921
6	(3,0)	13.745	13.638	10.457	10.207	8.658	8.246
7	(2,1)	10.970	10.818	8.017	7.7189	6.598	6.168
8	(3,1)	N.A.	N.A.	N.A.	N.A.	-5.638	-4.755
9	(4,0)	N.A.	N.A.	N.A.	N.A.	-8.511	-7.173
-9	-(4,0)	N.A.	N.A.	N.A.	N.A.	-25.340	-32.801
-8	-(3,1)	N.A.	N.A.	N.A.	N.A.	-25.965	-35.219
-7	-(2,1)	-16.490	-16.800	-25.246	-27.297	-37.798	-46.142
-6	-(3,0)	-19.418	-19.620	-28.364	-29.785	-41.932	-48.220
-5	-(1,1)	-22.561	-22.909	-30.718	-32.822	-42.837	-50.895
-4	-(0,1)	-24.315	-24.564	-32.714	-34.390	-45.417	-52.325
-3	-(2,0)	-27.623	-27.889	-35.959	-37.595	-48.780	-55.331
-2	-(1,0)	-31.418	-31.730	-39.669	-41.367	-53.020	-58.980
-1	-(0,0)	-32.690	-32.901	-41.334	-42.528	-55.658	-60.122

Each mode of the PBE has an associated shape function, $\hat{p}_j$, (or structure) that determines the nulls and peaks of the pressure contribution from that mode in the 2D plane. The structure of some modes from a select few setpoints are presented here to identify some effects of the shear flow on acoustic propagation in the duct. The most cut-on mode of the PBE corresponds to the plane-wave mode of the CHE. In Fig. 6, it may be observed that the shape function corresponding to κ_1 is uniform across the 2D plane for the case of $f = 600$ Hz and $M_c = 0.3$. This uniformity coincides with the structure of the plane wave CHE mode. As the frequency increases, along with the Mach number, refraction of the sound by the shear flow in the boundary layer region causes the pressure amplitude, and correspondingly the shape function, to become more concentrated along the walls of the duct. The most drastic case of this for the current investigation occurs when $f = 3000$ Hz and $M_c = 0.5$, as observed in Fig. 6c. Some asymmetry is present in the mode structure in Fig. 6c when comparing the bottom wall to the top wall. The cause of this asymmetry has yet to be explored, but will be investigated in future research. One potential contributing factor may be asymmetry in the bottom and top wall boundary layers, but any asymmetry, if present, has not been quantified.

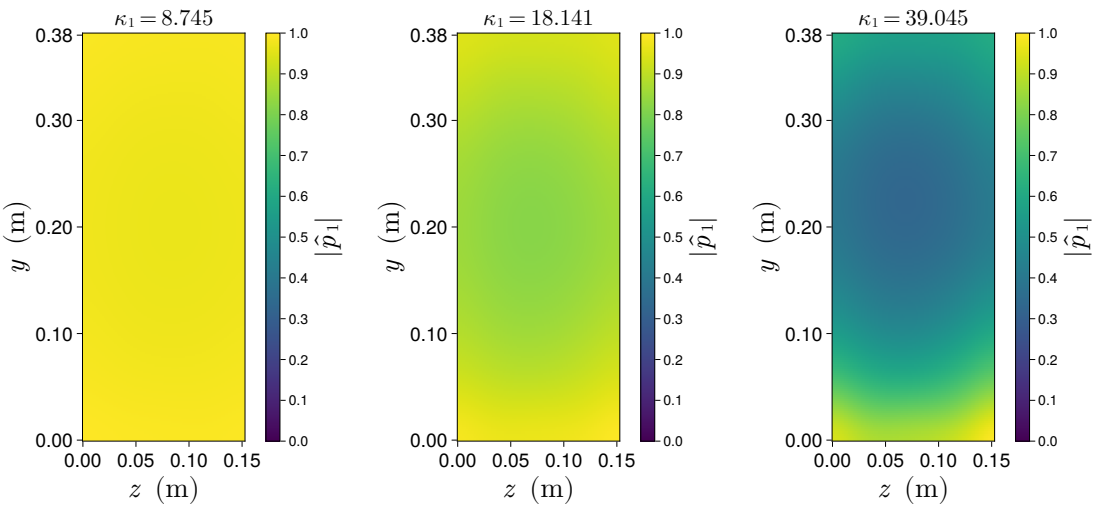

(a) **(b)** **(c)**

Fig. 6 Eigenfunctions corresponding to the first mode for the case of (a) $f = 600$ Hz and $M_c = 0.3$, (b) $f = 1400$ Hz and $M_c = 0.5$, and (c) $f = 3000$ Hz and $M_c = 0.5$.

The most cut-on mode, κ_1 (or κ_{-1}), appears to be most significantly impacted by the presence of shear flow, as opposed to the other modes present in the duct. This may be observed in Fig. 7, where Fig. 7a and Fig. 7d vary more considerably from the CHE result for the plane wave mode as opposed to the κ_2 and κ_3 modes, which adhere closely to the standard cosine structure of the $(1, 0)$ and $(2, 0)$ CHE modes. This finding appears to be in support of the results of the simulations of Savkar [20], which suggest that the lowest-order mode is most significantly affected by the shear flow. Although the mode structure of the lowest-order mode is more significantly impacted across the frequency range, the reconstruction errors presented in Fig. 5 do not appear to suggest that the accuracy of the solution is more greatly improved for κ_1 dominant setpoints.

The unique characteristic of the PBE modes is that the structure of the positive and negative modes will vary due to the effects of refraction, as opposed to the CHE modes. For instance, the κ_{-1} mode in Fig. 7d is amplified in the center of the duct, which is opposite of the κ_1 structure. This is due to the direction of propagation of the mode relative to the propagation direction of the flow. The propagation direction of the κ_{-1} mode opposes the direction of the flow; thus, refraction effects in the boundary layer cause the sound to bend away from the walls. The κ_1 mode, however, propagates along the direction of the flow, and the boundary layer has the effect of trapping sound near the walls. This is similar to the phenomenon of surface ducts in the field of ocean acoustics, and may also be observed in acoustic propagation in the atmosphere depending on the meteorological conditions.

The effect of boundary layer refraction on the most cut-on mode may have important consequences for the testing of acoustic liners as well. The reduced pressure amplitude near the walls in the case of acoustic propagation opposing the flow implies that the effectiveness of an impedance boundary in attenuating the signal may be reduced as compared to the case of acoustic propagation in the direction of flow. Additionally, impedance eduction methods based upon the CHE cannot account for this effect, and discrepancies may arise in the educed impedance of a liner that is exposed to sound of the same frequency and dominant mode structure in the same flow environment, but with different acoustic propagation directions. Methods based upon the 2D PBE will account for some of this effect; however, flows in typical acoustic liner test rigs are highly three-dimensional as a consequence of the small cross-sectional area, and 2D methods will suffer in accuracy from assumptions made regarding the flow profile.

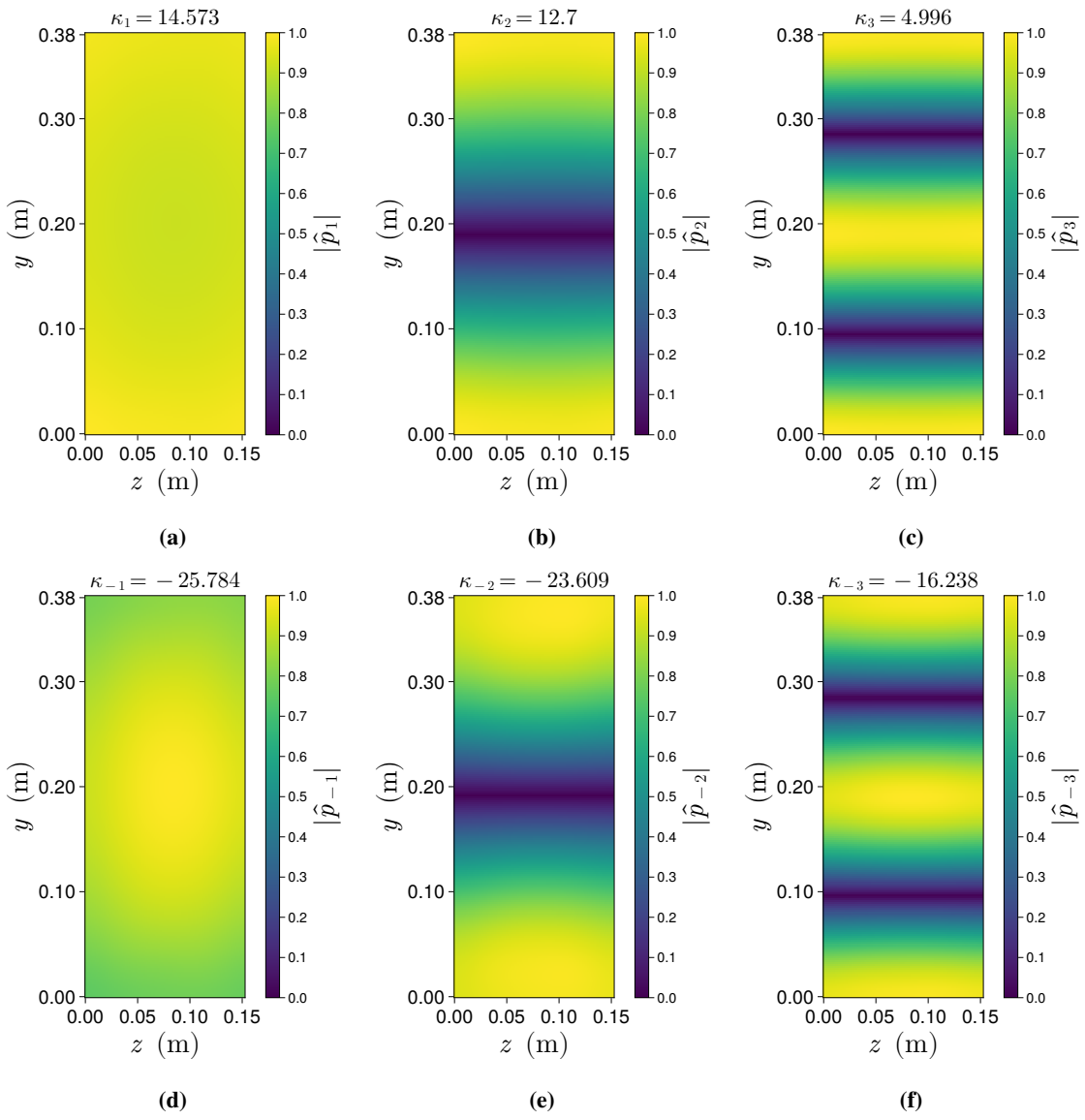

Fig. 7 Eigenfunctions corresponding to each mode for the case of f = 1000 Hz and M_c = 0.3.

As the frequency is increased, the structure of the higher-order modes may deviate quite significantly from the CHE mode structure. This may be clearly observed in Fig. 8, which presents 6 different higher-order modes for the case of f = 3000 Hz and M_c = 0.5. The mode κ_{24} is the highest-order positive mode that is cut-on in the duct, while κ_{14} represents a "middle-order" mode (for lack of a better term) and κ_4 is one of the lower-order modes present at this condition (corresponding to the (0, 1) CHE mode). Each positive mode in the figure is accompanied by its corresponding negative mode. The negative modes presented here display a drastically different structure than the positive modes, due to refraction effects. Surprisingly, even the highest-order modes at f = 3000 Hz and M_c = 0.5 are impacted by this phenomenon, which is in contrast to results at f = 1000 Hz and M_c = 0.3. Mode structure plots for an additional setpoint, f = 1600 Hz and M_c = 0.5, are shown in Fig. 11 in the Appendix. It is clear in Fig. 11 that the structures of all modes are impacted by refraction effects. Although the contour plots of every mode at each setpoint could not be included here, a survey of all mode structures indicates that the effects of refraction are present at every setpoint to varying degree. The magnitude to which the flow direction alters the positive and negative mode structures appears to depend on a combination of frequency, Mach number, and mode number, but it is not clear at this time which parameter is most sensitive.

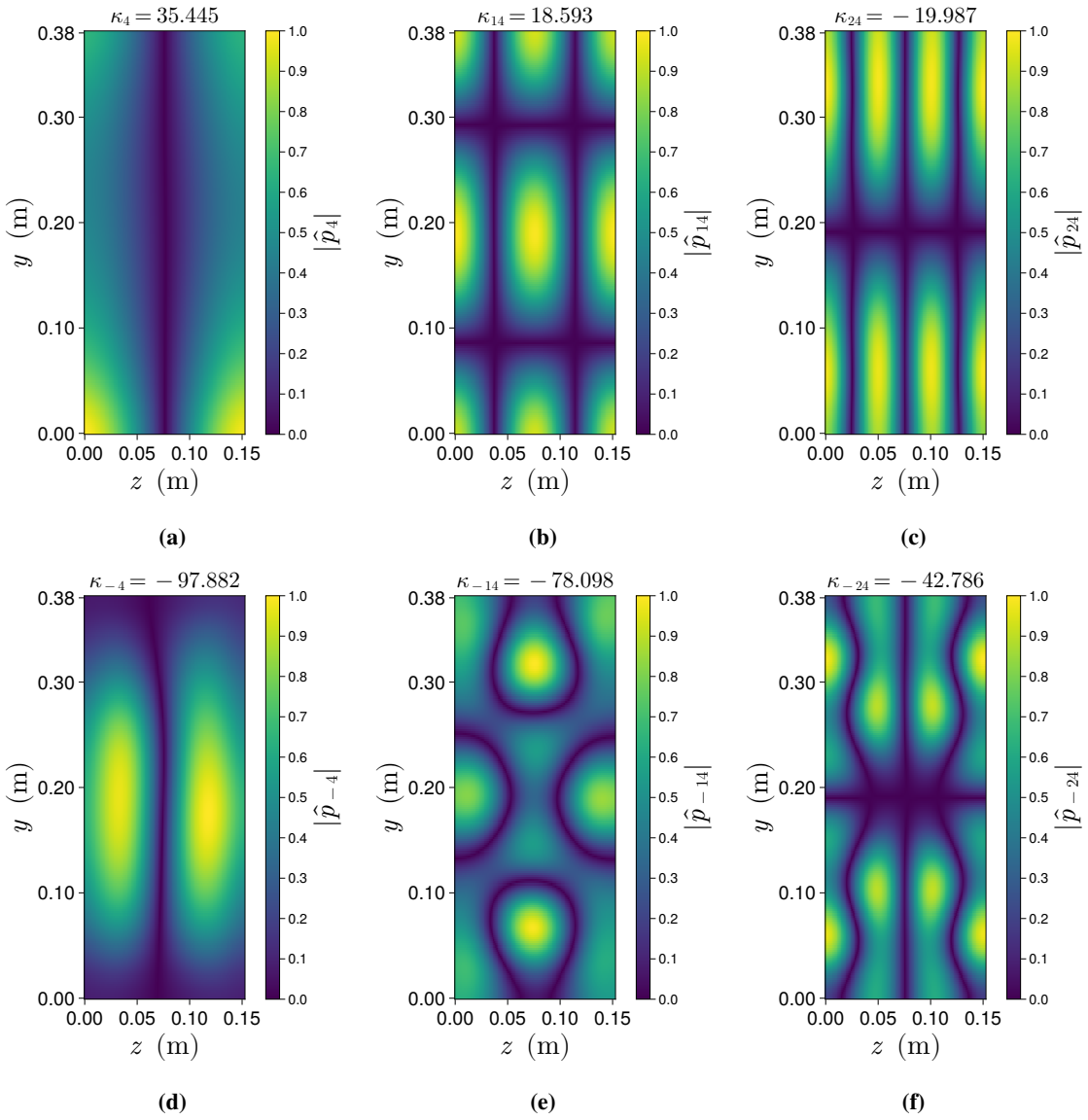

Fig. 8 Eigenfunctions corresponding to a few modes for the case of $f = 3000$ Hz and $M = 0.5$.

It should be noted that some higher-order modes at higher frequencies and centerline Mach numbers appeared out of order with respect to their positive (or negative) counterpart. This is exemplified in Fig. 9, where the structure of the κ_{22} mode corresponds to the structure of the κ_{-23} mode at $M_c = 0.5$ and $f = 3000$ Hz. It is unclear at this time if this is an error in the eigenvalue computation with the method of successive linear problems, or if this is a true physical result. Multiple tests were conducted with the method of successive linear problems, varying the tolerance of the residual and decreasing the step size between successive guesses of the eigenvalues, but neither parameter changed the order of the determined eigenvalues when altered. Although the cause of this effect is not known, for the modal decomposition performed here, the order of the eigenvalues do not affect the computations. Thus, this was not investigated further, and will be addressed in future investigations.

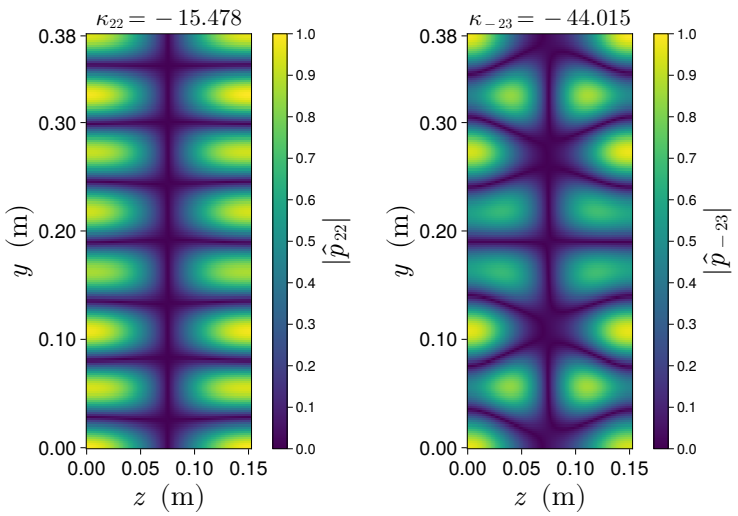

(a) **(b)**

Fig. 9 Eigenfunctions corresponding to the (a) κ_{22} mode and (b) κ_{-23} mode for $M_c = 0.5$ and $f = 3000$ Hz.

C. Mode Amplitudes from Acoustic Liner Test Samples

Two acoustic liner samples, CDTR3 and CDTR5, are tested at $M_c = 0.1$, 0.3, and 0.5 in the frequency range of 400 to 3000 Hz. The CDTR mode control algorithm is used to drive up CHE modes from the $(0, 0)$ to the $(1, 2)$ mode. The mode control algorithm has authority over a larger range of modes; however, this subset was chosen to reduce testing time and examine only modes present across multiple frequencies, so that frequency dependent trends could be assessed. Modal amplitude computed using PBE modes and CHE modes is compared across the range of frequencies for the cases when the $(0, 0)$ and $(0, 1)$ CHE modes are dominant in Fig. 10. For PBE modes in the downstream array, the assumption is made that the flow profile in that region matches the flow profile upstream of the test section. In Fig. 10, all of the results presented correspond to $M_c = 0.5$. In Figs. 10a and 10b, the PBE and CHE results are presented (respectively) for the lowest-order mode dominant ($(0, 0)$ or κ_1). The mode amplitudes of each result agree in both the upstream and downstream arrays to within ±0.25 dB.

Results for the $(0, 1)$ (or κ_4) mode dominant are presented in Figs. 10c and 10d for the PBE and CHE, respectively. In this case, the PBE mode amplitudes are about 1-2 dB higher in magnitude than the CHE modes. For other higher-order modes not displayed in Fig. 10, Table 3 shows the average value across all frequencies, and for both upstream and downstream arrays, of the difference in the mode SPL between the PBE modes and the CHE modes for each Mach number and liner sample. A positive value indicates that the PBE modes are on average higher in amplitude than the CHE modes, and vice-versa for a negative value. Table 3 shows that there is more disagreement in the higher-order mode amplitudes than there are for the $(0, 0)$ (or κ_1) mode amplitudes. Even though the average difference across all frequencies in the mode SPL for the lowest-order mode is small, as the frequency increases, the discrepancy in the mode SPL for this mode increases as well. At 3000 Hz, the upstream $(0, 0)$ CHE mode SPL is 0.63 dB higher in amplitude than the κ_1 PBE mode for the $M_c = 0.5$ CDTR3 setpoint. Thus, as frequency increases, the PBE mode decomposition is an improved approximation over the CHE mode decomposition, even for the lowest-order mode.

The improved microphone reconstruction errors presented in Sec. IV.A in the PBE reconstruction would imply that the mode amplitudes obtained by the PBE decomposition are likely more accurate. Thus, the CHE mode decomposition is less accurate for higher-order modes. The very similar results between CDTR3 and CDTR5 suggest that the differences are insensitive to the liner sample. There also appears to be no monotonically increasing trend of the differences as the mode number is increased, which would indicate that perhaps for certain modes the microphone placement is more favorable for a PBE modal decomposition, as opposed to a CHE method.

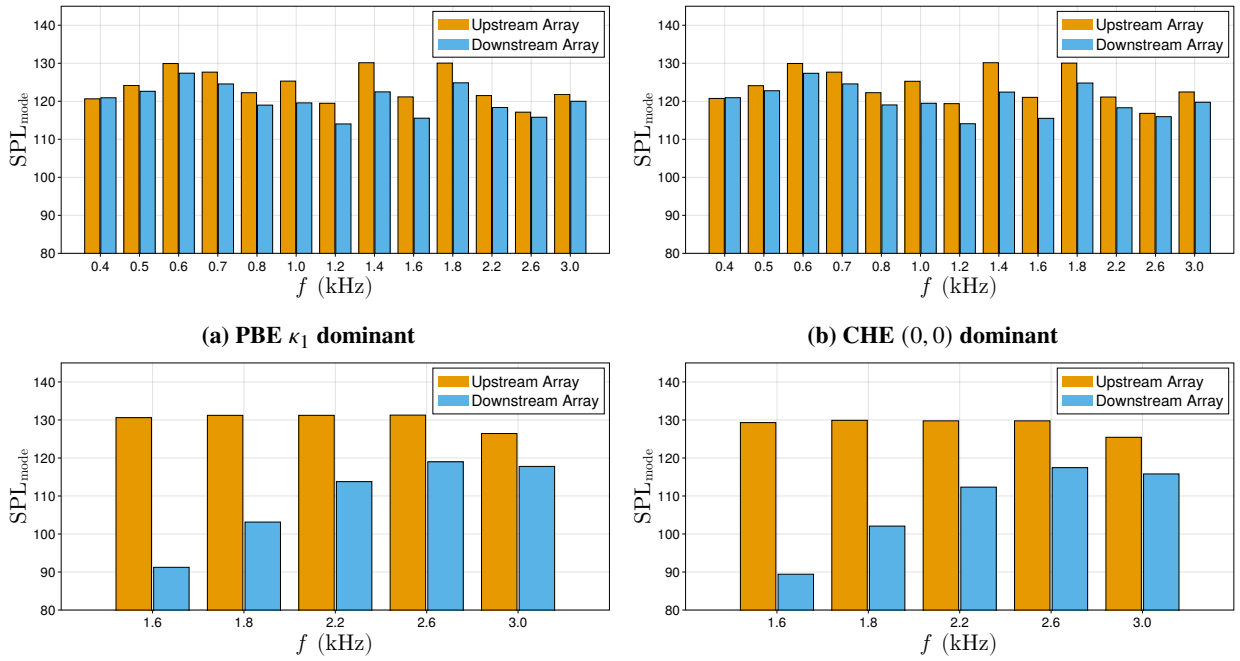

(a) PBE κ_1 dominant

(b) CHE $(0,0)$ dominant

(c) PBE κ_4 dominant

(d) CHE $(0,1)$ dominant

Fig. 10 Mode SPL computed in the upstream and downstream arrays for the CDTR3 sample for (a) PBE modes and (b) CHE modes with $(0,0)$ CHE mode dominant, and (c) PBE modes and (d) CHE modes with $(0,1)$ CHE mode dominant.

Table 3 Average mode SPL difference across frequencies between PBE and CHE modes for $M_c = 0.1$, 0.3, and 0.5 of the CDTR3 sample tests.

		Avg. SPL difference (dB) CDTR3			Avg. SPL difference (dB) CDTR5		
PBE mode	CHE mode	$M_c = 0.1$	$M_c = 0.3$	$M_c = 0.5$	$M_c = 0.1$	$M_c = 0.3$	$M_c = 0.5$
1	$(0,0)$	0.03	0.02	0.02	0.02	0.04	0.01
2	$(1,0)$	1.11	1.10	1.09	1.10	1.12	1.07
3	$(2,0)$	-0.26	-0.25	-0.12	-0.26	-0.24	-0.13
4	$(0,1)$	1.23	1.38	1.44	1.23	1.45	1.23
5	$(1,1)$	2.27	2.35	2.32	2.27	2.38	1.92
6	$(3,0)$	-1.82	-1.83	-1.86	-1.83	-1.82	-1.87
7	$(2,1)$	0.89	0.98	0.95	0.92	1.07	1.02
8	$(3,1)$	-0.63	-0.66	-0.61	-0.63	-0.58	-0.61
9	$(4,0)$	-3.80	-3.33	-3.88	-3.80	-3.32	-3.83
12	$(0,2)$	-0.03	0.06	0.26	-0.06	-0.07	0.36

The discrepancy between the modal amplitudes computed by the CHE and PBE methods for higher-order modes is in support of the arguments of Salikuddin and Ramakrishnan [18], that the higher-order modes are most affected by shear flow, apparently in contradiction to Savkar [20]. This investigation suggests that both points of view may be correct, when discussing certain specific details of the acoustic propagation. In one instance, the mode structure of the lowest-order mode is more significantly impacted by the boundary layer than the higher-order modes. On the other hand, the predicted mode amplitudes more significantly vary between the CHE and PBE results for higher-order modes. From a practical standpoint, when acoustic propagation is in the direction of the flow (downstream), the CHE mode decomposition appears to be a sufficient tool for acoustic fields where the lowest-order mode is dominant. More caution

is urged when using such an approximation at higher frequencies and flow speeds for acoustic fields with higher-order modes dominant.

V. Conclusion

The present investigation incorporated shear flow effects in the modal decomposition of acoustic signals present in the NASA Langley CDTR. When shear flow effects are accounted for, the reconstruction error between the computed modal fields and the microphone measurements is reduced when higher-order modes are dominant in the duct, implying an improved accuracy when using PBE modes. The structure of PBE modes are impacted by shear flow refraction effects. The lowest-order mode (corresponding to the CHE plane wave mode) is impacted by refraction effects across a wider range of frequencies than the higher-order modes. As frequency and Mach number are increased, the higher-order mode structures lose symmetry between the positive and negative modes due to the effect that the flow direction has on the bending of wavefronts in the shear layer for opposing acoustic propagation directions. Finally, modal amplitudes computed with both the PBE and CHE approaches for two sample liners show that differences in the mode SPL appear between the two approaches, although these differences are likely not significant for most engineering purposes.

Presently, a considerable amount of liner design and optimization is performed assuming infinitesimal boundary layers with the Ingard-Myers boundary condition. As the bypass ratio of commercial aircraft engines increases, the allowable area for acoustic liner installation may become more constrained. Thus, improvements to the design and optimization process of liners may be required to maintain acoustic performance. One such improvement could be the incorporation of shear flow effects from a predicted Reynolds averaged Navier-Stokes mean flow in propagation codes used to optimize liner impedance in the aft or inlet duct of turbofan engines. In this situation, a no-slip boundary condition for the mean flow would be satisfied at the impedance wall. Thus, any acoustic liner designed to match this impedance will have to be verified by experiment with data processing techniques that account for shear flow appropriately. The work presented here represents the beginning stages of incorporating 3D shear flow effects in liner impedance eduction.

Future investigations will focus on further improving the methods and approach presented here for robustness and extension to liner impedance eduction. A flow survey downstream of the test section will be the first step to improving this process in the CDTR, and was originally planned for this investigation but could not be performed due to a fan bearing seal failure. As discussed in Sec. IV.A, the method of successive linear problems missed a cut-on eigenvalue at $M_c = 0.5$ and $f = 2200$ Hz, and there is no guarantee that the method will find the maximal number of eigenvalues for any setpoint. Thus, further investigation must examine ways to make the method more robust, or replace this approach with another technique, such as the contour integral method [27], to ensure that the maximal number of eigenvalues are computed. Development of liner impedance eduction capabilities with 3D shear flow effects would support future flow direction impedance studies and improved impedance optimization tools. Currently, the GFIT is the main rig for impedance eduction in grazing flow environments at NASA Langley Research Center. Testing conditions are limited to plane-wave frequencies, which correspond to less than around 3000 Hz. Further development of the techniques presented here may enable the GFIT to operate above the plane-wave frequency for impedance eduction.

Appendix

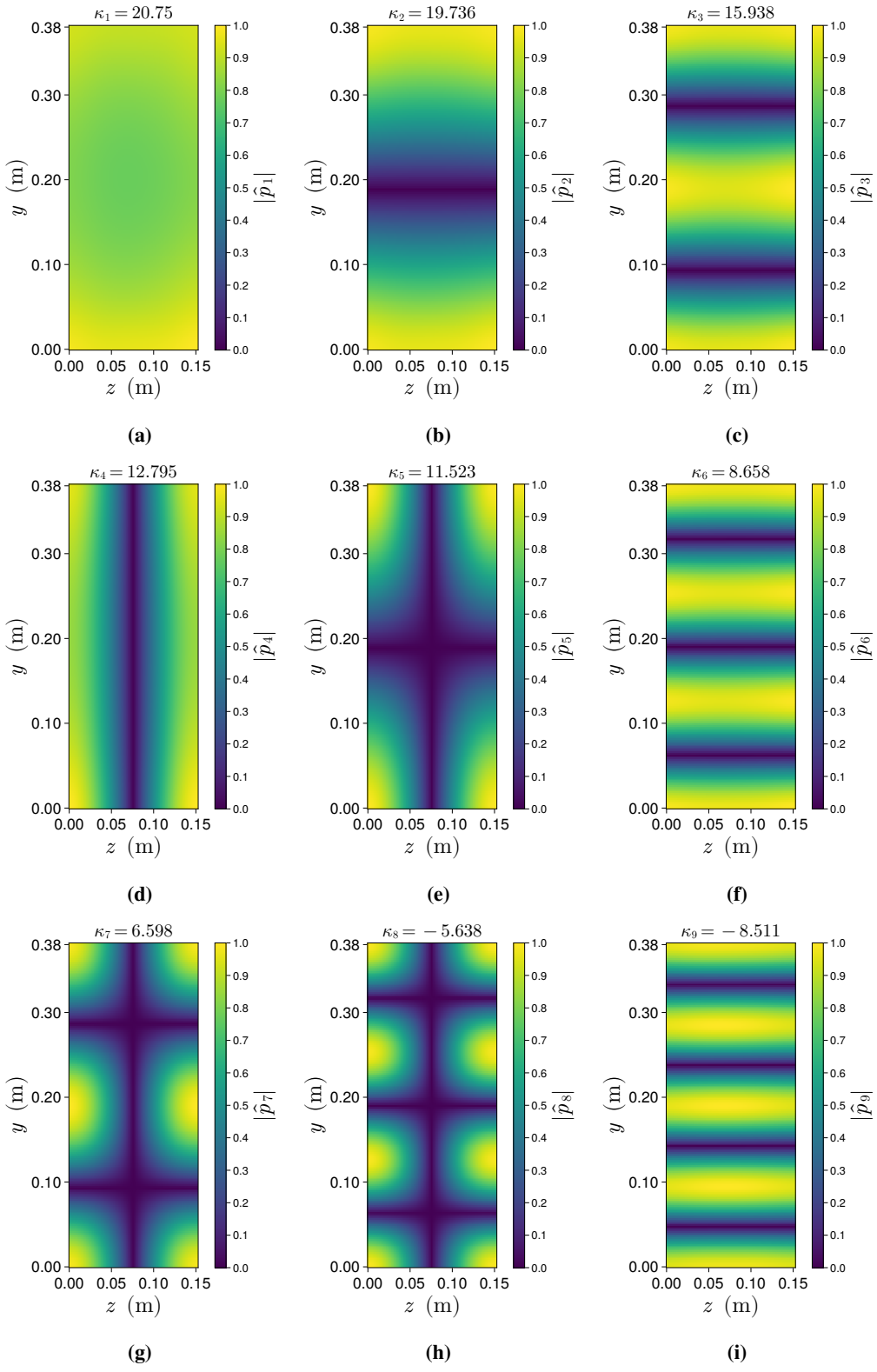

Fig. 11 Eigenfunctions corresponding to each mode for the case of $f = 1600$ Hz and $M_c = 0.5$.

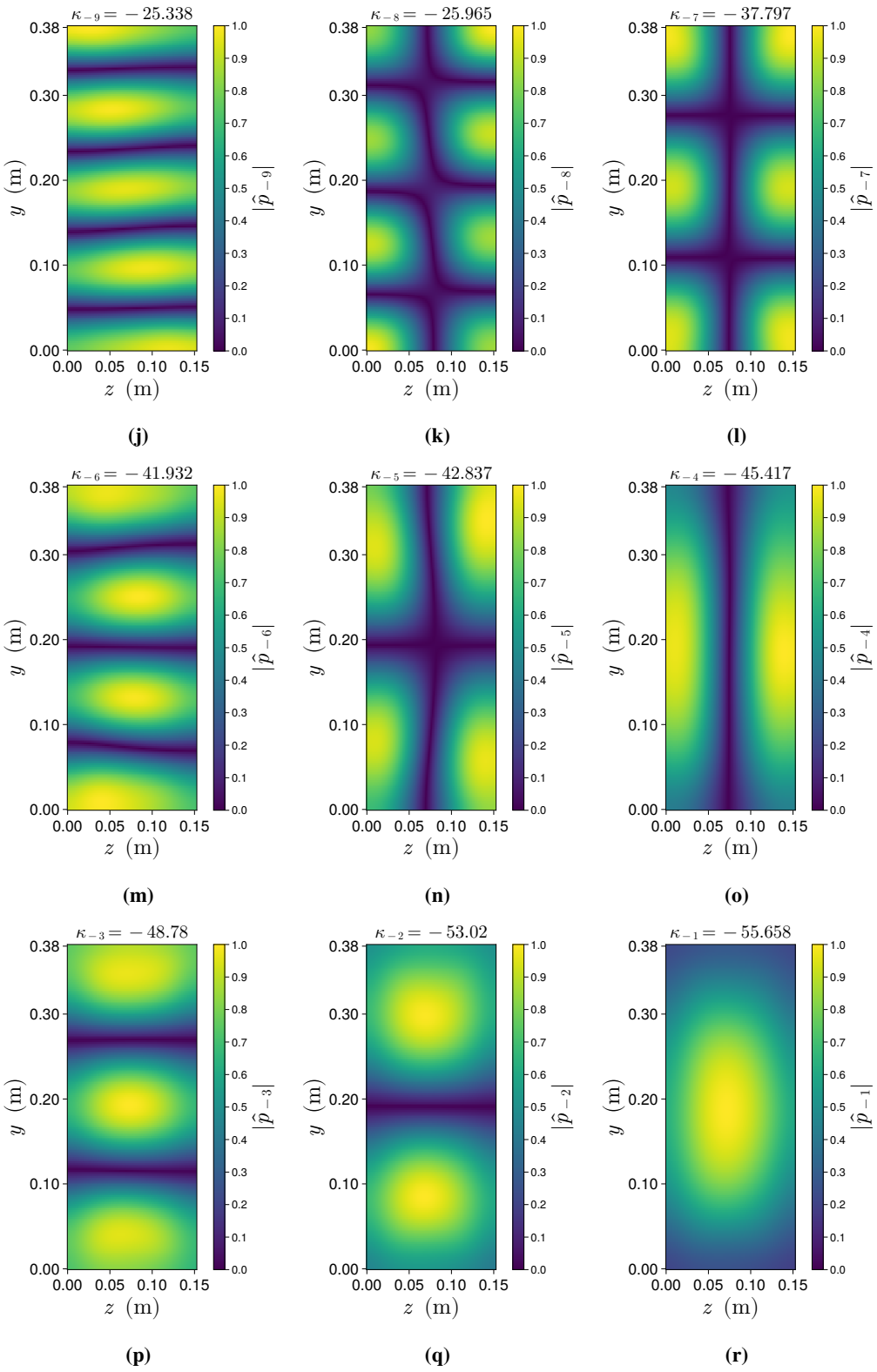

Fig. 11 (Cont.) Eigenfunctions corresponding to each mode for the case of $f = 1600$ Hz and $M_c = 0.5$.

Acknowledgments

A. N. Carr would like to thank Dr. Douglas Nark and Mr. Michael Jones for fruitful discussions regarding flow direction effects on educed impedance. Additionally, Dr. Nark provided additional insight on the use of NURBS for creating 2D surfaces of the Mach number profiles and provided a previously developed software tool to perform this task. A. N. Carr would also like to thank Mr. Brian Howerton for his previous work in integrating the CHE modal decomposition software into the CDTR mode control software. Additional appreciation is extended to Mrs. Martha Brown and Mr. Max Reid for their support during testing in the CDTR. This work was funded by the Advanced Air Transport Technology Project under the Advanced Air Vehicles Program at the National Aeronautics and Space Administration.

References

[1] Ingard, U., "Influence of fluid motion past a plane boundary on sound reflection, absorption, and transmission," *The Journal of the Acoustical Society of America*, Vol. 31, No. 7, 1959, pp. 1035–1036. https://doi.org/10.1121/1.1907805.

[2] Myers, M., "On the acoustic boundary condition in the presence of flow," *Journal of Sound and Vibration*, Vol. 71, No. 3, 1980, pp. 429–434. https://doi.org/10.1016/0022-460X(80)90424-1.

[3] Brambley, E. J., "Well-posed boundary condition for acoustic liners in straight ducts with flow," *AIAA Journal*, Vol. 49, No. 6, 2011, pp. 1272–1282. https://doi.org/10.2514/1.j050723.

[4] Rienstra, S. W., and Darau, M., "Boundary-layer thickness effects of the hydrodynamic instability along an impedance wall," *Journal of Fluid Mechanics*, Vol. 671, 2011, p. 559–573. https://doi.org/10.1017/S0022112010006051.

[5] Watson, W. R., and Jones, M. G., "Impedance eduction in a duct using linearized Euler equations," *2018 AIAA/CEAS Aeroacoustics Conference*, AIAA 2018-3442, Atlanta, Georgia, 2018. https://doi.org/10.2514/6.2018-3442.

[6] Watson, W. R., Carpenter, M. H., and Jones, M. G., "Performance of Kumaresan and Tufts algorithm in liner impedance eduction with flow," *AIAA Journal*, Vol. 53, No. 4, 2015, pp. 1091–1102. https://doi.org/10.2514/1.J053705.

[7] Schulz, A., Weng, C., Bake, F., Enghardt, L., and Ronneberger, D., "Modeling of liner impedance with grazing shear flow using a new momentum transfer boundary condition," *23rd AIAA/CEAS Aeroacoustics Conference*, AIAA 2017-3377, Denver, Colorado, 2017. https://doi.org/10.2514/6.2017-3377.

[8] Zhang, P., Huang, Y., Yang, Z., Yang, C., and Jiang, W., "Effect of source direction on liner impedance eduction with consideration of shear flow," *Applied Acoustics*, Vol. 183, No. 108297, 2021. https://doi.org/10.1016/j.apacoust.2021.108297.

[9] Nark, D. M., Jones, M. G., and Piot, E., "Assessment of axial wave number and mean flow uncertainty on acoustic liner impedance eduction," *2018 AIAA/CEAS Aeroacoustics Conference*, AIAA 2018-3444, Atlanta, Georgia, 2018. https://doi.org/10.2514/6.2018-3444.

[10] Åbom, M., "Modal decomposition in ducts based on transfer function measurements between microphone pairs," *Journal of Sound and Vibration*, Vol. 135, No. 1, 1989, pp. 95–114. https://doi.org/10.1016/0022-460X(89)90757-8.

[11] Mugridge, B., "The measurement of spinning acoustic modes generated in an axial flow fan," *Journal of Sound and Vibration*, Vol. 10, No. 2, 1969, pp. 227–246. https://doi.org/10.1016/0022-460X(69)90198-9.

[12] Harel, P., and Perulli, M., "Measurement, in a duct, of the space-structure of the discrete-frequency noise generated by an axial compressor," *Journal of Sound and Vibration*, Vol. 23, No. 4, 1972, pp. 487–498. https://doi.org/10.1016/0022-460X(72)90505-6.

[13] Bolleter, U., and Crocker, M. J., "Theory and measurement of modal spectra in hard-walled cylindrical ducts," *The Journal of the Acoustical Society of America*, Vol. 51, No. 5A, 1972, pp. 1439–1447. https://doi.org/10.1121/1.1912994.

[14] Moore, C. J., "In-duct investigation of subsonic fan "rotor alone" noise," *The Journal of the Acoustical Society of America*, Vol. 51, No. 5A, 1972, pp. 1471–1482. https://doi.org/10.1121/1.1912997.

[15] Pickett, G. F., Sofrin, T. G., and Wells, R. A., "Method of fan sound mode structure determination final report," Tech. Rep. NASA-CR-135293, 1977.

[16] Kerschen, E., and Johnston, J., "A modal separation measurement technique for broadband noise propagating inside circular ducts," *Journal of Sound and Vibration*, Vol. 76, No. 4, 1981, pp. 499–515. https://doi.org/10.1016/0022-460X(81)90266-2.

[17] Pasqualini, J. P., Ville, J. M., and de Belleval, J. F., "Development of a method of determining the transverse wave structure in a rigid wall axisymmetric duct," *The Journal of the Acoustical Society of America*, Vol. 77, No. 5, 1985, pp. 1921–1926. https://doi.org/10.1121/1.391836.

[18] Salikuddin, M., and Ramakrishnan, R., "Acoustic power measurement for single and annular stream duct-nozzle systems utilizing a modal decomposition scheme," *Journal of Sound and Vibration*, Vol. 113, No. 3, 1987, pp. 441–472. https://doi.org/10.1016/S0022-460X(87)80132-3.

[19] Schultz, T., Cattafesta, L. N., and Sheplak, M., "Modal decomposition method for acoustic impedance testing in square ducts," *The Journal of the Acoustical Society of America*, Vol. 120, No. 6, 2006, pp. 3750–3758. https://doi.org/10.1121/1.2360423.

[20] Savkar, S., "Propagation of sound in ducts with shear flow," *Journal of Sound and Vibration*, Vol. 19, No. 3, 1971, pp. 355–372. https://doi.org/10.1016/0022-460X(71)90695-X.

[21] Boucheron, R., Bailliet, H., and Valiere, J.-C., "Analytical solution of multimodal acoustic propagation in circular ducts with laminar mean flow profile," *Journal of Sound and Vibration*, Vol. 292, No. 3, 2006, pp. 504–518. https://doi.org/https://doi.org/10.1016/j.jsv.2005.08.017, URL https://www.sciencedirect.com/science/article/pii/S0022460X05006073.

[22] Nark, D. M., and Jones, M. G., "A fundamental study of bifurcation acoustic treatment effects on aft-fan engine noise," *AIAA AVIATION 2023 Forum*, AIAA 2023-3345, San Diego, CA and Online, 2023. https://doi.org/10.2514/6.2023-3345.

[23] Pridmore-Brown, D. C., "Sound propagation in a fluid flowing through an attenuating duct," *Journal of Fluid Mechanics*, Vol. 4, No. 4, 1958, pp. 393–406. https://doi.org/10.1017/S0022112058000537.

[24] Rienstra, S. W., "Numerical and asymptotic solutions of the Pridmore-Brown equation," *AIAA Journal*, Vol. 58, No. 7, 2020, pp. 3001–3018. https://doi.org/10.2514/1.J059140.

[25] Mehrmann, V., and Voss, H., "Nonlinear eigenvalue problems: a challenge for modern eigenvalue methods," *GAMM-Mitteilungen*, Vol. 27, No. 2, 2004, pp. 121–152. https://doi.org/10.1002/gamm.201490007.

[26] Ruhe, A., "Algorithms for the nonlinear eigenvalue problem," *SIAM Journal on Numerical Analysis*, Vol. 10, No. 4, 1973, pp. 674–689. https://doi.org/https://doi.org/10.1137/0710059.

[27] Beyn, W.-J., "An integral method for solving nonlinear eigenvalue problems," *Linear Algebra and its Applications*, Vol. 436, No. 10, 2012, pp. 3839–3863. https://doi.org/10.1016/j.laa.2011.03.030.

[28] Blackstock, D. T., *Fundamentals of physical acoustics*, John Wiley & Sons, Nashville, TN, 2000.